Citation: Lockett, R. D. & Bonifacio, A. (2019). Hydrodynamic Luminescence in a Model Diesel Injector Return Valve. International Journal of Engine Research, 22(3), pp. 963-974. doi: 10.1177/1468087419870421

Hydrodynamic Luminescence in a Model Diesel Injector Return Valve

***R.D. Lockett, A. Bonifacio**

Department of Mechanical Engineering & Aeronautics, City, University of London, Northampton Square, London, UK

*Corresponding Author

Email: r.d.lockett@city.ac.uk

Abstract

A sample of unadditized diesel fuel was passed through an optically accessible model diesel injector return valve, which consisted of two successive nozzles connected to an intermediate fuel gallery. The first nozzle was cylindrical, while the second nozzle was stepped. The fuel was observed to produce a multi-phase, cavitating flow and a luminous blue-violet emission at the entrance to the second nozzle hole. The flow in the upstream intermediate fuel gallery and the first nozzle hole remained single-phase. Spectral analysis of the luminous emission revealed a spectrum with thermal features containing broad spectral lines and peaks at 358 nm, 389 nm, 405 nm, 412 nm, 430 nm and 475 nm, suggesting that the emission was dominated by $\pi^* \rightarrow \pi$ transitions in the alkylated mono-, di-, and tri-aromatics, with additional spectral contributions from CH, C_2, C_3 and hydrogen (H).

Keywords

Diesel, flow, cavitation, hydro-luminescence, spectrum, spectroscopy

1. Introduction

Most modern diesel fuel injection equipment (FIE) consist of a high pressure pump feeding diesel fuel to fuel injectors via a common pressure accumulator (often termed a common rail) [1 – 3]. The injectors are required to be capable of providing precise quantities of fuel to the engine in multiple injections [2, 3]. This is achieved through the provision of high, stable fuel pressures of up to 2,500 bar to 3,000 bar in the pressure accumulator (common rail) [4 – 6]. Most diesel injectors are of the multi-hole type, commonly supplied in a 6-hole, 8-hole, 9-hole or 12-hole configuration, with convergent passages and profiled hole inlets. This is to maintain high discharge efficiency by reducing the choking effect of geometric film cavitation on the nozzle flow, and to support improved atomization [7, 8]. The activation of the injectors is either direct, through the injector needle being connected to a piezo-electric stack (piezo injector) [9], or indirect, through magnetic solenoid activation of a ferromagnetic pushrod, supported by an internal 2- or 3-nozzle internal pressure control system (solenoid injector) [10, 11]. Most commercial injectors are of the magnetic solenoid type, due to the combination of relatively low cost and long-term reliability.

The electrical activation of the magnetic solenoid produces a lift force on the pushrod. Once the pushrod has lifted, the pressure in the upper fuel gallery surrounding the pushrod is low, and the fuel flow to the gallery is choked by the pressure control nozzles. The difference in fuel pressure between the fuel in the lower fuel gallery at the bottom of the injector relative to the fuel surrounding the pushrod at the top of the injector provides the force necessary to support the lift of the injector needle against the restoring force supplied by the needle spring. The upper pushrod is returned to its closed position once the magnetic solenoid is switched off, which causes the fuel pressure inside the injector to equilibrate at the accumulator supply pressure, resulting in the injector needle returning to its sealed position at the end-of-injection.

The diesel injectors internal pressure control system therefore returns a significant fraction of diesel fuel supplied to the injectors back to the fuel tank via control nozzles. Additional fuel metering occurs in the high-pressure fuel pump, which involves passing surplus fuel compressed in the pump back to the fuel tank via metering control nozzles. This recycling of fuel from the high-pressure fuel injection equipment (FIE) back to the tank via control nozzles may impose stress on the fuel, resulting in premature fuel ageing and degradation [12, 13]. The flows occurring across such nozzles develop large pressure gradients in the neighbourhood of sharply curved surfaces (at the entrance to the nozzle holes and at the nozzle step, for example), producing regions with very low local fluid pressure. If the local diesel fluid pressure falls below the local saturated vapour pressure, then vapour cavities are able to form and grow around the many nucleation sites travelling in the fluid (nano-particles or gas bubbles), or located on the nozzle surface (surface irregularities). Given the very large pressure gradients occurring across the control nozzles in diesel fuel injection equipment, the multi-phase flow that develops results in the growth of multiple, closely spaced fuel vapour bubbles which merge to form bubble clouds (cloud cavitation). If the bubble cloud develops adjacent to an enclosure surface, then the bubble cloud will often develop into a vapour film or sheet (termed film/sheet cavitation) [14, 15].

Ultrasonic cavitation is known to produce sono-chemical reactions in alkanes and diesel fuel, resulting in C-C and C-H bond cleavage in the alkanes and aromatics that comprise the diesel [16 – 18]. A further industry study of the effect of ultrasonic cavitation on diesel fuel showed that the ultrasonic excitation produced sono-chemical pyrolysis reactions that led to the formation of sticky black gums and soot-like nano-particles and aggregated particulates [13]. In parallel with this, Jeshani [19], Fatmi [20], and Lockett *et al*. [12, 21, 22] have investigated the effect of hydrodynamic cavitation in diesel nozzles on diesel fuel. This work employed time-resolved in-situ measurements of the optical attenuation coefficient of various diesel fuel samples as a function of cavitation exposure time, together with 2-column gas chromatography (2-D GCxGC) measurements of the composition of samples obtained before and after cavitation, and ultraviolet-visible (uv-vis) absorption spectrophotometry.

The in-situ optical attenuation measurements show that nozzle cavitation produced a change in diesel fuel composition in all of the diesel samples tested. 2-D GCxGC and particle analysis of the fuel samples obtained before and after cavitation showed a consistent decrease in mono-aromatic and di-aromatic concentration, together with a corresponding increase in particle concentration [19]. Analysis of uv-visible absorption spectra obtained from similar experiments conducted later produced finding that were consistent with the earlier measurements [20]. A detailed analysis of 2-D GCxGC spectra obtained from fresh and cavitated fuel samples showed that the naphthenic mono-aromatics were particularly susceptible to hydrodynamic sono-chemical destruction, to form polycyclic aromatic hydrocarbons and primary soot-like nano-particles.

This paper is an extension of the previous work on the effect of hydrodynamic cavitation on diesel fuel. An optically accessible, fused silica model of the internal pressure control system located inside magnetic solenoid operated diesel injectors was employed to characterize the flow occurring in the pressure control nozzles. In the course of this characterization, it was discovered that the diesel flowing into the second nozzle produced a luminous emission of blue-violet light for upstream and downstream pressures in excess of 180 bar and ambient respectively. This paper reports the results of an optical examination of this luminous emission.

2. Experimental Setup

2.1 High-Pressure Recirculating Flow Rig

A customised, high-pressure recirculating flow rig was designed and manufactured at City, University of London, for the purpose of investigating the effect of high pressure nozzle flow on diesel. It consists of a 3.0 l fuel tank supplying diesel to a high-pressure diesel fuel pump via a rotary vane feed pump and fuel filter. The high-pressure pump supplied the diesel to a customised nozzle via a diesel pressure accumulator (common rail) at pre-determined pressures ranging from 200 bar up to 1,700 bar. The nozzle flow was stagnated in a receiver, which resulted in a large fuel temperature rise through the conversion of pump compression energy to internal energy. The high temperature fuel leaving the receiver was then returned back to the fuel tank via a shell-and-tube heat exchanger, which was used to maintain the low-pressure fuel temperature at a pre-determined value (typically 55^{o}C or 70^{o}C). A small fraction of the fuel passing through the recirculating flow rig could be diverted to an optically accessible cell for continuous in-situ measurements of optical attenuation coefficient of the diesel fuel samples. Figure 1 shows the layout of the high-pressure recirculating flow rig.

{Please place Figure 1 here}

2.2 Fused Silica Nozzle Assembly

2.2.1 Background

A number of in-service magnetic solenoid operated commercial diesel injectors representing the major diesel fuel injection equipment manufacturers (Denso, R. Bosch GMBH etc.) were procured, stripped down and inspected, in order to reveal the design for injector operation and control. During this inspection, it was discovered that the internal fuel pressure control and needle lift systems had similar designs, and operated in a similar manner to each other. Figure

2 shows a schematic of a typical, generic, magnetic solenoid actuated diesel injector. Essentially, the upper pressure control system consisted of two successive nozzles connecting the high pressure fuel inlet to the low pressure fuel return gallery via an intermediate fuel gallery. The diameter of the first nozzle, the injector needle spring constant, and the fuel pressure in the intermediate fuel gallery determines the dynamical response of the injector needle in lift and return. The high pressure nozzle was approximately 0.200 mm in diameter and 1.0 mm long in the commercial injectors subjected to strip-down and inspection. In most cases, the second nozzle was stepped, with a nozzle length and initial diameter of approximately 1.0 mm and 0.22 mm respectively, increasing to 0.4 mm to 0.5 mm diameter at the step. In all cases, the injector pushrod had a conical end that was employed to seal the second stepped nozzle at the large diameter end.

{Please place Figure 2 here}

The two-nozzle pressure control system located either side of an internal fuel gallery is employed to control the rate of change of fuel pressure in the upper part of the injector, containing the intermediate and low pressure fuel galleries, pushrod and fuel return. The two-nozzle pressure control system also ensures a smooth, single phase flow into the intermediate pressure gallery, displacing the nozzle cavitation to the nozzle step in the second nozzle [23, 24].

2.2.2 Fused Silica Sections

An optically accessible replica diesel injector pressure control system that reflected the flow characteristics and pressure distribution occurring inside actual diesel injectors was designed and manufactured using fused silica sections that were supported by a stainless-steel cage. The fused silica model pressure control system was designed to employ two processed rectangular fused silica blocks with 40.0 mm length sides and 14.0 mm height arranged in series. Figures 3 (a) and (b) show the design schematics for the two fused silica sections.

{Please place Figures 3 (a) and (b) here}

The first high pressure block had a 7.0 mm diameter cylindrical bore 4.1 mm deep, ending in a 4.06 mm radius of curvature hemispherical section on the upstream high-pressure end, and a 7.0 mm diameter, 3.4 mm deep bore, ending with a 4.06 mm radius of curvature hemispherical section on the intermediate pressure end of the block. The two bored sections of the block were connected by a 0.20 mm diameter, 1.61 mm long nozzle hole. The second low pressure block had a 7.0 mm diameter bore 3.4 mm deep, ending with a 4.06 mm radius of curvature hemispherical section on the intermediate pressure end, and a 10.0 mm diameter bore 2.86 mm deep, ending with a conical section converging to a point 1.96 mm deep on the low pressure end of the block. The two bored sections of the block were connected by a stepped nozzle hole of 0.22 mm initial diameter and 1.61 mm length, increasing to 0.30 mm diameter and 0.97 mm length.

The two blocks were aligned in a series configuration, and compressed together using 1.0 mm thick nitryl gaskets. The intermediate pressure chamber formed through the series alignment of the two fused silica sections was sealed using a 6.5 mm diameter, 6.0 mm long stainless-steel sleeve fitted with two nitryl o-rings. The bored section on the high-pressure side of the upstream fused silica element was sealed using a similar sleeve-o-ring arrangement.

2.2.3 Stainless-Steel Cage and Needle

The two fused silica elements were placed inside a stainless-steel cage, providing a clear side-view optical access to the interior nozzles and hemispherical recesses. The upper part of the cage had a fine-threaded screw attached to a needle fitted with a bearing and PTFE cone at the lower end, in order to provide a needle seal and needle lift to the low-pressure conical section, similar to those occurring in commercial injectors. The adjustment screw had a calibrated circular head with 25 measurement division markers (14.4^{o} between markers). A full turn of the control screw lifted the needle by 0.25 mm (10 μm needle lift per division marker).

The base of the cage assembly contained a 6 mm threaded high-pressure fitting (rated to 700 bar) to connect the pipe carrying the high pressure diesel fuel from the pressure accumulator (common rail) to the nozzle assembly. Figure 4 shows the schematic side-view drawing of the fused silica assembly in the stainless-steel cage, with the needle screw adjustment knob at the top.

{Please place Figure 4 here}

2.3 Camera Arrangement

A Nikon D7000 DSLR camera reverse coupled to a Nikon manual focus AI-s 50 mm f/1.2 lens via a set of 86 mm long extension tubes was employed to take high-resolution photographs of the hydrodynamic luminescence produced by the diesel flow entering the second nozzle from the intermediate pressure fuel gallery. The extension tube and lens assembly produced images with a magnification of 2.709 (image resolution of 1.765 μm/pixel). Images of the luminescence were obtained using a fixed f/1.2 aperture setting, with various exposure settings ranging from 1.0 ms exposure duration to 12.5 ms exposure duration.

2.4 High-Speed Video

A monochrome Photron FASTCAM SA1.1 high-speed video camera reverse coupled to a Nikon manual focus AI-s 50 mm f/1.2 lens via a set of 204 mm long extension tubes was employed to take high speed video of the hydrodynamic luminescence produced by the diesel flow entering the second nozzle from the intermediate pressure fuel gallery. The extension tube and lens assembly produced video images with a magnification of 4.82 (image resolution of 4.15 µm/pixel). High speed video of the luminescence was obtained at 2 kHz using a fixed f/1.2 aperture setting, with an exposure duration of 0.5 ms. Figure 5 shows a photograph of the high speed Photron Fastcam SA1.1 video camera with the reverse-coupled Nikon 50 mm f/1.2 lens and lens extension, focused on the hydrodynamic luminescence originating from the second nozzle of the fused silica model injector pressure control system. Unfortunately, the camera failed to self-calibrate properly during operation, resulting in a number of pixels not responding to the incident luminescence.

{Please place Figure 5 here}

2.5 Spectrometer

A 50 mm diameter, bi-convex, coated, uv-grade fused silica lens of 10.0 cm focal length (f/2.0) with an object and image distance of 20.0 cm (optical magnification of 1.0) was employed to capture and focus the hydrodynamic luminescence occurring in the 2nd nozzle onto a Newport-Oriel MS125 1/8 m f/3.7 spectrometer. The spectrometer employed a 0.200 mm wide slit, 2400 line/mm Richardson grating (wavelength range 180 nm – 600 nm, with 275 nm blaze wavelength) and Model 78855 linear CCD array sensor (2048x1 pixel), producing a spectral resolution and dispersion of 0.5 nm and 0.036 nm/pixel respectively at 400 nm wavelength.

Consequently, the diffracted signal incident on the detector was subjected to 4x1 binning, resulting in an effective dispersion of 0.1185 nm/binned pixel at 450 nm wavelength, increasing to 0.1440 nm/binned pixel at 400 nm, and increasing again to 0.1657 nm/binned pixel at 350 nm wavelength. The spectrometer was calibrated using a Newport-Oriel 78812 Mercury-Argon Hg(Ar) calibration set. Figure 6 shows a photograph of the Nikon D7000 DSLR camera and 50 mm f/1.2 lens reverse-coupled to 86 mm long lens extension tubes, and the Newport Oriel MS125 spectrometer and linear CCD array sensor. Both are focused on capturing the hydrodynamic luminescence originating from the second nozzle of the fused silica model injector pressure control system.

{Please place Figure 6 here}

3. Experimental Method

The high-pressure recirculating flow rig was filled with approximately 3.3 l of fresh unadditized middle distillate diesel fuel. The needle in the fused silica assembly was adjusted to approximately 2.0 mm lift, in order to ensure free, unchoked flow in the low-pressure conical receiver. The low-pressure feed pump was switched to circulate the diesel fuel around the rig. Once the rig was filled with diesel, the high-pressure pump was turned on and slowly adjusted to produce an accumulator pressure of approximately 240 bar. The hydrodynamic luminescence was observed to begin with irregular flickering at the entrance to the 2nd nozzle hole at approximately 170 bar – 200 bar accumulator pressure. A further increase in pressure resulted in a continuous luminous emission of blue-violet light from the entrance to the 2nd nozzle hole. The lights in the laboratory were left on during the procurement of the DSLR camera photographs. The lens aperture was set to its maximum value of f/1.2 (42 mm aperture), and the exposure duration varied between 1.0 ms and 12.5 ms. Multiple images were obtained at each exposure. The large lens aperture, together with the large magnification, defines a small depth of field.

The lights in the laboratory were turned off, prior to the procurement of the luminescence emission data on the high-speed video camera and the spectrometer. This was to minimise contamination of the high-speed video images and the spectrometer signal obtained from the luminescence by background light. This was followed by the procurement of the high-speed video data at 2 kHz and the spectral data via the spectrometer linear array sensor. The Photron Fastcam SA1.1 high-speed monochrome video camera was controlled by proprietary software (Photron PFV), which controlled the triggering, timing, sampling frequency and exposure, amongst others. Initially, background images of the field of view without luminous emission were obtained at 2 kHz frequency with an exposure of 0.5 ms (reduced accumulator pressure). This was followed by (1) an increase in the accumulator pressure to 240 bar to achieve steady-state luminous emission from the flow, and (2) procurement of high speed video of the hydrodynamic luminescence at a frequency of 2 kHz and exposure of 0.5 ms.

The Newport Oriel Model 78855 Linear CCD Array sensor was controlled by proprietary software provided by Newport Optics (Linespec Basic). The full width of the binned 512x1 pixel sensor covered a spectral range of approximately 60.7 nm at 450 nm central wavelength, increasing to approximately 73.7 nm at 400 nm and 84.8 nm at 350 nm central wavelength. Each dataset that was procured involved a number of steps, which are summarized here: (1) the luminous emission reaching the spectrometer slit was blocked, (2) 5 mean background scans were obtained by taking the mean of 50 scans of 5 ms exposure duration for each wavelength range selected (252 nm – 342 nm, 303 nm – 388 nm, 360 nm – 434 nm, 414 nm – 475 nm, and 465 nm – 520 nm), (3) the luminous emission from the flow entering the 2nd nozzle was unblocked, permitting the light to enter the 0.2 mm wide slit entrance to the spectrometer, via the 50 mm diameter focussing lens, and (4) 5 mean spectra of the luminous emission were obtained by taking the mean of 50 scans of 5 ms exposure duration for each wavelength range selected. Finally, the optical response of the spectrometer and sensor alignment was measured.

4. Results and Discussion

A multi-phase cavitating flow was observed to form at the entrance to the second, stepped nozzle hole. No multiphase flow was observed to occur in the optically accessible region of the model return valve inside and upstream of the intermediate fuel gallery. In a previous experiment using a paraffinic model diesel, a multi-phase cavitating flow was observed to form at the entrance to the second nozzle for overall upstream to downstream pressure ratios greater than 4.0 [23, 24]. The first nozzle had a diameter of 0.200 mm, while the second, stepped nozzle had an initial diameter of 0.220 mm, increasing to 0.300 mm at the step. The cavitation number in flows of this type can be defined to be

$$C_N = \frac{\frac{1}{2}\rho v_B^2}{p_{back} - p_{sat}(T)} = \frac{p_{upstream} - p_{back}}{p_{back} - p_{sat}(T)} \tag{1}$$

where $p_{upstream}$, p_{back}, and $p_{sat}(T)$ are the upstream fuel pressure, the downstream fuel pressure and the saturated vapour pressure at flow temperature T respectively. The corresponding overall critical cavitation number for cavitation inception was estimated to be approximately 4.0 ± 0.1 in this nozzle using the paraffinic model diesel. It is expected that the critical cavitation number for cavitation inception for crude oil derived middle distillate diesel would be similar to the above value.

In this experiment, the upstream accumulator pressure was raised to 240 bar, while the downstream pressure was maintained at ambient pressure (~ 1.0 atm). Flickering luminescence was observed to occur at the entrance to the second nozzle passage for an accumulator pressure range of approximately 160 bar – 180 bar. The luminescence emission appeared to steady once the accumulator pressure rose above 220 bar. Consequently, an accumulator pressure of 240 bar was selected for these imaging and spectroscopy measurements. This produced a cavitating flow in the second nozzle with an overall cavitation number $C_N \approx 239$.

{Please place Figure 7 here}

Figure 7 shows a photograph of the hydrodynamic luminescence obtained at the entrance of the second nozzle, extending approximately 1.0 mm along the nozzle passage. The photograph of the second nozzle has a magnification of 2.709, with a transverse spatial resolution of 1.765 μm/pixel. The photographic image was obtained with an aperture and exposure duration of f/1.2 and 12.5 ms respectively. The first part of the second nozzle had a diameter of 0.220 mm (125 pixels), increasing to 0.300 mm (170 pixels) at the step. The yellow light originating from the hemispherical section upstream of the nozzle originates from the yellow diesel fuel in the intermediate fuel gallery.

The photograph presented in Figure 7 reveals that the diesel flow has produced a blue-white luminous emission located immediately downstream of the entrance to the second nozzle. The emission intensity was relatively uniform over a 200 μm length, followed by a decreasing conical signal with low signal along the central axis, extending approximately 1.0 mm along the nozzle hole. The 2 kHz high-speed video produced video image frame data that was consistent with the photographic images, showing luminous emission occurring immediately downstream of the second nozzle entrance, followed by a decreasing conical signal with low signal along the central axis, extending approximately 1.0 mm along the nozzle hole. The conical signal was observed to exhibit time-dependent spatial fluctuation, which is considered to be a consequence of fluctuations occurring in the nozzle flow due to cavitation and turbulence.

Figure 8 shows a false colour image of the mean luminescence obtained by the monochrome Photron FASTCAM SA1.1 video camera, together with the corresponding colour bar. The mean image was obtained from 1,000 image frames taken successively at 2 kHz, each with an exposure duration of 0.50 ms. The mean luminescence image shows the very rapid drop-off of the captured luminescence signal as a function of distance along the nozzle axis. The mean signal in the neighbourhood of the nozzle entrance was approximately 2,684 counts per exposure, while the signal in the conical region dropped to approximately 250 counts per exposure.

An inspection of the mean hydro- luminescence image shown in Figure 8 reveals a cloud of low intensity signal surrounding the high intensity signal. This was caused by a combination of imperfect optical focussing and the leakage of photo-electrons from the illuminated pixels to surrounding pixels (electronic noise) during exposure and readout. The mean image was excessively grainy due to the failure of the CMOS sensor array to properly re-calibrate itself before and during exposure and readout.

{Please place Figure 8 here}

Figure 9 shows a false colour image of the corresponding standard deviation obtained from the 1,000 image frames recorded on the Photron SA1.1 camera. As with the mean luminescence emission image shown in Figure 8, the standard deviation image shown in Figure 9 was also excessively grainy. The standard deviation of the temporal variation of luminescence intensity in the neighbourhood of the nozzle entrance was approximately 111 counts, while the standard deviation in the conical region was approximately 37 counts. The image ratio of standard deviation to mean scales the spatial variability of the luminescence with time. $\bar{s}_{ij}/\bar{I}_{ij} \sim 0.041$ in the neighbourhood of the nozzle entrance, and $\bar{s}_{ij}/\bar{I}_{ij} \sim 0.147$ in the conical region, where s_{ij} and I_{ij} were the standard deviation of and the mean of the luminescence signal at the row i, column j pixel respectively.

{Please place Figure 9 here}

Figure 10 shows a graph of the mean emission spectrum as a function of emission wavelength that has been obtained from the nozzle flow by the MS125 spectrometer and linear array sensor. The spectrum has been measured and processed over a wavelength range of 300 nm to 475 nm, and has been corrected for offset, background light, instrument dispersion and optical response. The mean spectrum contains six broad bands, with the band maxima occurring at 350.8 nm, 370.3 nm, 389.8 nm, 410.4 nm, 431.0 nm, and 456.8 nm. The spectrum represents the aggregate emission obtained from the diesel flowing through the second nozzle, which appears to contain both thermal and species-specific components.

{Please place Figure 10 here}

The six dominant bands contributing to the emission lie in the near-ultra-violet to visible blue part of the electromagnetic spectrum. Excited species H, CH, CH_3, C_2, C_3, some mono-aromatics, di-aromatics, tri-aromatics, phenyls and their radicals emit fluorescence light in this range of wavelengths. These are likely to be the major contributors to the aggregate mean spectrum. For example, the small band located at the top of the global maximum at 389.8 nm to 390.0 nm is most likely to be the $B^2\Sigma^- \rightarrow X^2\Pi$ transition of excited CH radicals [25]. CH radical emission is also likely to be present in the fifth band (425 nm – 435 nm) through the $A^2\Delta \rightarrow X^2\Pi$ transition at 431.0 nm [25, 26]. Emission from hydrogen atoms (H) are likely to contribute to the observed spectrum through the Balmer Series at 383.54 nm (9 → 2), 388.90 nm (8 → 2), 397.00 nm (7 → 2), 410.17 nm (6 → 2), 434.05 nm (5 → 2), and 486.13 nm (4 → 2). C_2 produces broad ro-vibrational emission bands at 360 nm, 385 nm, 410 nm, 436 nm, 470 nm, 473 nm and 516 nm [25, 26]. C_3 produces a broad emission band over the 397 nm to 410 nm range of wavelengths [27]. Azulene produces a broad emission band over the 350 nm to 400 nm range of wavelengths [28]. Naphthalene, Methylnaphthalene, Dimethylnaphthalene, Acenaphthene, and Phenylnaphthalene produce broad emission bands over the 320 nm to 380 nm range of wavelengths [28]. Various Diphenylnaphthalenes have broad emission bands over the 340 nm to 460 nm range of wavelengths [28]. Anthracene, Methylanthracene, Phenylanthracene, Diphenylanthracene, Phenanthrene, Chrysene, Triphenylene and low concentrations of Pyrene have broad emission bands over the 350 nm to 450 nm range of wavelengths [28]. All of the aromatic emission bands present in the measured spectrum (Figure 8) are likely to be combinations of the three spin-allowed $\pi^* \rightarrow \pi$ transitions ($^1E_{1u} \rightarrow {}^1A_{1g}$, $^1B_{1u} \rightarrow {}^1A_{1g}$, and $^1B_{2u} \rightarrow {}^1A_{1g}$), subjected to bathochromic shifting through extended orbital conjugation.

Crude oil derived diesel typically contains approximately 70% – 75% paraffins (comprised of approximately 50% open-chain paraffins and 50% naphthenes), 25% mono-aromatics (comprised of approximately 50% alkylated mono-aromatics and 50% naphthenic mono-aromatics), 3% – 4% di-aromatics (comprised of alkylated naphthalenes, naphthenic naphthalenes and phenyls), and 1% tri-aromatics (alkylated anthracenes and phenyls) [29]. The diesel sample employed in this study has been subjected to a 2-column gas chromatography analysis, which has separated the molecular components and identified the relative fractions of hydrocarbon classes comprising the diesel [20]. The gas chromatogram defining the composition of the diesel sample employed in this experiment is shown in Figure **11**, revealing that the sample was composed of approximately 38% open-chain paraffins, 37% naphthenes (75% paraffins), 11% alkylated mono-aromatics, 9% naphthenic mono-aromatics (20% mono-aromatics), 3.5% alkylated di-aromatics, 0.5% naphthenic di-aromatics (4% di-aromatics) and 1.0% tri-aromatics.

{Please place Figure 11 here}

The hydrodynamic luminescence observed at the entrance to the second nozzle has two possible known mechanisms. These are electro-luminescence (tribological in origin) and sono-luminescence. Electro-luminescence is the emission of ultraviolet and visible electromagnetic radiation originating in the fluid due to electronic excitation and possible electrical breakdown occurring as a result of molecular/atomic ionization and ion/electron transfer from the fluid to the surrounding medium in response to the formation of an intense electric field at the sharp edge entrance to the nozzle hole [30 – 33]. The electro-luminescence signal is dependent on the stability of the electric field that sustains it, that is likely to be relatively steady-state for a steady flow around the sharp edge defining the transition from the hemispherical end of the intermediate fuel gallery to the 0.220 mm nozzle hole passage.

Sono-luminescence is the emission of ultraviolet and visible radiation that occurs during cavitation bubble collapse [34 – 37]. It occurs through the excitation of electronic states and/or ionization of the atoms and molecules of vapour comprising the collapsing bubbles that occurs as a consequence of the work that the surrounding fluid does on the bubble’s constituent molecules/atoms during bubble collapse. It is expected, therefore, that the main source of sono-luminescence radiation is likely to be displaced a short distance downstream of the entrance to the nozzle holes. Furthermore, it is expected that the sono-luminescence will reflect the frequency and intensity of bubble collapse, that is likely to exhibit radiation frequency- and time-based variability.

The steady-state character and local homogeneity of the luminous emission immediately downstream of the nozzle hole suggests that this emission was caused by electro-luminescence (alternatively termed tribo-luminescence), rather than sono-luminescence. Margulis and Pil’gunov have examined the electrical breakdown and luminescence emitted from oil and water flows through narrow channels (nozzles) formed in metals and organic glass (polymethyl methacrylate) [30, 31]. This was supported by an analysis of the potential difference, electric field and discharge current responsible for sustaining the luminescence. They measured the luminescence spectra and compared them to emission spectra originating from other mechanisms, concluding that the origin of the luminescence was tribological (electrical breakdown downstream of the sharp edge through frictional/shear effects at the boundary). In this analysis, they have estimated the streaming electric current i, steady-state electric charge

Q and electric field strength E sustaining the luminous emission in the liquid layer adjacent to the passage to be

$$i = \frac{-\varepsilon\pi R^2 p \int_0^R \left(\frac{d^2\phi}{dr^2} + \frac{1}{r}\frac{d\phi}{dr}\right) dr}{\mu l} \tag{2}$$

$$Q = \frac{\pi\varepsilon^2 R^2 p \lambda_0 \int_0^R \left(\frac{d^2\phi}{dr^2} + \frac{1}{r}\frac{d\phi}{dr}\right) dr}{\mu l} \tag{3}$$

$$E = \frac{\varepsilon R p \lambda_0 \int_0^R \left(\frac{d^2\phi}{dr^2} + \frac{1}{r}\frac{d\phi}{dr}\right) dr}{4\mu l^2} \tag{4}$$

where ε is the liquid electrical permittivity, R is the radius of the passage, p is the upstream liquid pressure, λ_0 is the liquid electrical resistivity, ϕ is the electro-kinetic potential sustaining the luminescence layer in the passage, μ is the liquid viscosity, and l is the length of the luminescence layer along the passage [31].

The model employed by Margulis and Pil'gunov [31] was based on the double electric layer model developed to explain the formation of electric charge distributions, electric fields and streaming currents observed to occur in dielectric oils flowing through narrow cooling channels in electrical machinery and oil refinery equipment [38 - 41]. This model suggests that impurity ionic and/or polar molecules imbedded in the dielectric fluid separate into their constituent ions. The model further suggests that the negative ions attach themselves to the wall of the flow channel, leaving the positively charged dielectric fluid to produce a streaming current through the concurrent flow of the positively charged ions. The charge distributions and consequent electric fields that were observed to form in these flows were, in some cases, able to produce dielectric breakdown. However, when dielectric breakdown was observed, it was observed to occur at long distances downstream of the channel entrance. Consequently, the double electric layer model may not be an appropriate model to describe the electromagnetic effects and luminous emission obtained from the multi-phase flow occurring immediately downstream of the nozzle entrance in this and other similar experiments [30, 31].

While the hydro-luminescence observed at the entrance to the nozzle hole is likely to be tribological in origin, the same cannot be claimed for the weaker, hollow cone shaped luminescence observed further downstream of the passage entrance. This luminescence may be sono-luminescence, originating through cavitation bubble/cloud collapse occurring 0.30 mm – 1.00 mm downstream of the entrance to the nozzle passage, in the recovering flow. However, the authors believe that the relatively weak, conically shaped, hydro-luminescence emission occurring downstream of the nozzle entrance was also tribological in origin, caused by the optical decay of excited molecules imbedded in the recovering flow, downstream of the tribological dielectric breakdown/excitation occurring in the nozzle hole near the nozzle entrance.

While this experiment has reported hydrodynamic luminescence obtained from diesel fuel in fused silica nozzles, those reported by Margulis and Pil’gunov [30, 31] have employed mineral oil and water flows in optically accessible acrylic nozzles in an acrylic flow vessel to produce hydro-luminescence. Mitroglou and Gavaises have also observed erratic hydro-luminescence pulses originating from diesel flowing through acrylic nozzles with lower upstream pressures (~ 50 bar) [42].

Margulis and Pil’gunov have confirmed that similar electric field generation has been observed to occur in high-pressure flows through metal nozzles [30, 31]. This, together with the accompanying hydrodynamic cavitation occurring in the nozzle, is likely to lead to tribological-and cavitation-induced chemical reactions in the diesel fuel employed in this experiment. Indeed, these processes may be responsible for the pyrolysis-like reactions observed in high-pressure cavitated/recirculated diesel reported by Jeshani [19] and Fatmi [20].

5. Conclusion

An optically accessible model diesel injector pressure control system has been developed and installed in a high-pressure diesel recirculation flow rig in order to investigate the character of the diesel flow occurring in the nozzles, the intermediate fuel gallery and the low pressure fuel return chamber. In the course of this investigation, hydrodynamic luminescence was observed to occur immediately downstream of the entrance to the second nozzle hole. In relation to this, the following conclusions may be drawn:

1. Hydrodynamic luminescence was observed to originate at the entrance to the second nozzle hole once the accumulator pressure exceeded 180 bar. In order to obtain relatively steady-state luminescence, the accumulator pressure was set to 240 bar.

2. High resolution single-shot images and high-speed video of the hydrodynamic luminescence were obtained using a digital single lens reflex camera and a monochrome high-speed video camera. They revealed that the luminescence originated at the entrance to the second nozzle hole, remaining of steady intensity for approximately 0.20 mm downstream of the nozzle entrance, followed by a decreasing conical signal extending approximately 1.0 mm downstream of the nozzle entrance. The hydrodynamic luminescence appeared blue-white to the naked eye and in the photographs.

3. The hydrodynamic luminescence emission was subjected to spectral analysis using a commercial spectrophotometer. The mean spectrum was observed to contain six broad bands, with the band maxima occurring at 350.8 nm, 370.3 nm, 389.8 nm, 410.4 nm, 431.0 nm, and 456.8 nm. The spectrum appeared to contain both a broadband thermal profile (most probably originating from free electrons) and species-specific elements. The species-specific contributions to the mean spectrum are believed to originate from atomic hydrogen, radicals CH, di-carbon (C_2) and tri-carbon (C_3), with the major contribution originating from the three broad-band spin-allowed $\pi^* \rightarrow \pi$ transitions in the many mono-cyclic, di-cyclic, tri-cyclic aromatics, and phenyls comprising the 25% aromatic content of the diesel.

4. It was hypothesized that the hydrodynamic luminescence occurring immediately downstream of the nozzle entrance was likely to be tribological (frictional electric field excitation and breakdown) in origin, rather than bubble cloud sono-luminescence. The location, extension and steady-state character of the luminescence supports this hypothesis. However, the origin of the hollow cone-shaped luminescence occurring further downstream of the nozzle entrance is uncertain; it may have been caused by the decay of excited molecules imbedded in the recovering flow. Alternatively, it may be sono-luminescence, caused through collapse of the cavitation bubble cloud in the bubbly multi-phase flow during fluid pressure recovery.

5. The hydrodynamic luminescence observed to occur in the nozzle flow suggests that the diesel passing through such a pressure control system may be subject to chemical degradation through tribology-induced and/or cavitation-induced pyrolysis reactions.

Acknowledgements

The authors acknowledge Shell Global Solutions for funding this work, and City, University of London technical staff Messrs Grant Clow, Jim Ford and Robert Cherry for their contributions to the manufacture and maintenance of the rig.

References

1. Stumpp, G. and Ricco, M., “Common Rail - An Attractive Fuel Injection System for Passenger Car DI Diesel Engines”, SAE Technical Paper 960870 (1996). https://doi.org/10.4271/960870.

2. Guerrassi, N. and Dupraz, P., “A Common Rail Injection System For High Speed Direct Injection Diesel Engines”, SAE Technical Paper 980803 (1998). https://doi.org/10.4271/980803.

3. Oki, M., Matsumoto, S., Toyoshima, Y., Ishisaka, K. et al., “180MPa Piezo Common Rail System”, SAE Technical Paper 2006-01-0274 (2006). https://doi.org/10.4271/2006-01-0274.

4. Mahr B., “Future and Potential of Diesel Injection Systems”. In: Whitelaw J.H., Payri F., Arcoumanis C., Desantes J.M. (eds) *Thermo- and Fluid Dynamic Processes in Diesel Engines 2*. Springer, Berlin, Heidelberg.(2004). https://doi.org/10.1007/978-3-662-10502-3_1

5. Shinohara Y, Takeuchi K., Herrmann O., Laumen H., “Mixture Formation – 3000 Bar Common Rail System”, *54417963-MTZ-Worldwide* Vol. 72(1) (2011) 4 – 9, Springer Shinohara.

6. Graham M., Keeler N. and Kewley J., “Ultra-high Pressure Common Rail Systems”, *Injection Systems for IC Engines*, IMechE, London, 13 – 14 May 2009, pp. 231 – 243, Chandos Publishing, ISBN 9781843345619.

7. Andriotis A., Gavaises M., Arcoumanis C., “Vortex flow and cavitation in diesel injector nozzles”, *Journal of Fluid Mechanics* 610 (2008) 195 – 215. https://doi.org/10.1017/S0022112008002668.

8. Javier Lopez J, de la Garza OA, De La Morena J, Martinez-Martinez S, “Effects of cavitation in common-rail diesel nozzles on the mixing process”, *International Journal of Engine Research* 18:10 (2017) pp. 1017 – 1034. https://doi.org/10.1177/1468087417697759

9. H. Kyu, S. Sung Wook Park, C. Sik Leea, “Effect of piezo-driven injection system on the macroscopic and microscopic atomization characteristics of diesel fuel spray”, *Fuel* 86(17 – 18) (2007) 2833 – 2845. https://doi.org/10.1016/j.fuel.2007.03.015.

10. Bianchi, G., Pelloni, P., Filicori, F., and Vannini, G., “Optimization of the Solenoid Valve Behavior in Common-Rail Injection Systems”, SAE Technical Paper 2000-01-2042 (2000). https://doi.org/10.4271/2000-01-2042.

11. Boehner, W. and Hummel, K., “Common Rail Injection System for Commercial Diesel Vehicles”, SAE Technical Paper 970345 (1997). https://doi.org/10.4271/970345.

12. Lockett R., Jeshani M., “An experimental investigation into the effect of hydrodynamic cavitation on diesel”, *International Journal of Engine Research* Vol. 14(6) (2013) pp. 606 – 621. https://doi.org/10.1177/1468087413497005.

13. Price R., Blazina D., Smith C., Davies T., "Understanding the impact of cavitation on hydrocarbons in the middle distillate range", *Fuel* 156 (2015) pp. 30 – 39. https://doi.org/10.1016/j.fuel.2015.04.026.

14. Franc J-P, Michel J-M, Chapter 8, Fundamentals of Cavitation, Kluwer Academic Publishers (2005), ISBN: 1-4020-2232-8.

15. Brennen CE, Chapter 7, Cavitation and Bubble Dynamics, Cambridge University Press (2014) ISBN: 978-1-107-64476-2.

16. Suslick KS, Gawienowski JJ, Schubert PF and Wang HH, "Alkane sonochemistry", *Journal of Physical Chemistry* 87(13) (1983) pp. 2299–2301. https://doi.org/10.1021/j100236a013.

17. Price GJ and McCollom M. "The effect of high-intensity ultrasound on diesel fuels", *Ultrasonic Sonochemistry* 2(2) (1995) S67–S70. https://doi.org/10.1016/1350-4177(95)00027-4.

18. Price GJ and McCollom M. "Use of high-intensity ultrasound as a potential test method for diesel fuel stability", *Fuel* 74(9) (1995) pp. 1394–1397. https://doi.org/10.1016/0016-2361(95)00084-I .

19. Jeshani M, "Optical Characterization of Cavitating Flows in Diesel Fuel Injection Equipment", PhD Thesis, City, University of London (2014).

20. Fatmi Z, "Optical and Chemical Characterization of the Effects of High-Pressure Hydrodynamic Cavitation on Diesel Fuel", PhD Thesis, City, University of London (2018).

21. Lockett RD, Fatmi Z, Kuti O, Price R, "An Investigation into the Effect of Hydrodynamic Cavitation on Diesel using Optical Extinction", *Journal of Physics: Conference Series* 656 (2015) 012091. https://doi.org/10.1088/1742-6596/656/1/012091.

22. Lockett R, Fatmi Z, Kuti O, Price R, "An Optical Characterization of the Effect of High-Pressure Hydrodynamic Cavitation on Diesel", SAE Technical Paper 2016-01-0841 (2016), https://doi.org/10.4271/2016-01-0841.

23. Bonifacio A, "An Optical Characterization and Modelling of Return Valve Flow in Diesel Fuel Injection Equipment", PhD Thesis, City, University of London (2019).

24. Bonifacio A, Lockett RD, Price, R, "Cavitating Flow in a Model Diesel Injector Return Valve", Paper CAV18-05032, ASME Proceedings of the 10th International Symposium on Cavitation, Baltimore, USA, May 2018, ISBN: 9780791861851. https://doi.org/10.1115/1.861851_ch31.

25. Herzberg G, The Spectra and Structures of Simple Free Radicals, Dover Publication Inc (1971). ISBN 978-0-486-65821-6.

26. Herzberg G, Molecular Spectra and Molecular Structure Volume I – Spectra of Diatomic Molecules, Krieger Publishing Company (1950) ISBN 0-89464-268-5.

27. Herzberg G, Molecular Spectra and Molecular Structure Volume III – Electronic Spectra and Electronic Structure of Polyatomic Molecules, Krieger Publishing Company (1950) ISBN 0-89464-270-7.

28. Berlman IB, Handbook of Fluorescence Spectra of Aromatic Molecules (2nd Edition), Academic Press (1971). ISBN 978-0-12-092656-5 https://doi.org/B978-0-12-092656-5.X5001-1.

29. Erwin J. Assay of diesel fuel components properties and performance. In: Symposium on processing and product selectivity of synthetic fuels, Division of Fuel Chemistry, American Chemical Society, Washington, USA, 23–28 August 1992, pp. 1915–1923.

30. Margulis MA and Pil'gunov VN, "Luminescence and Electrification in a Flow of Dielectric Liquids through Narrow Channels", *Russian Journal of Physical Chemistry A* 83 (8) (2009) pp. 1414 – 1418. https://doi.org/10.1134/S0036024409080287.

31. Margulis MA and Pil'gunov VN, "The Mechanism of the Appearance of Luminescence and Electrification in Liquid Flows through Narrow Channels", *Russian Journal of Physical Chemistry A* 83 (10) (2009) pp. 1789 – 1793. https://doi.org/10.1134/S0036024409100288.

32. Biryukov DA and Gerasimov DN, "Spectroscopic diagnostics of hydrodynamic luminescence", *Journal of Molecule Liquids* 266 (2018) pp. 75 – 81. https://doi.org/10.1016/j.molliq.2018.06.043.

33. Editors Olawale DO, Okoli OO, Fontenot RS, Hollerman WA, Authors Biryukov DA and Gerasimov DN, Chapter 5: Triboluminescence of Liquid Dielectrics: On a Way to Discover the Nature of Sonoluminescence, in Book Triboluminescence – Theory, Synthesis, and Application, Springer (2016), ISBN 978-3-319-38841-0. https://doi.org/10.1007/978-3-319-38842-7.

34. Editors: Crum LA, Mason TJ, Reisse JL and Suslick KS, Sonochemistry and Sonoluminescence: Proceedings of the NATO Advanced Study Institute on Sonochemistry and Sonoluminescence, Springer Science+Business Media Dordrecht (1997) ISBN 978-90-481-5162-2. https://doi.org/10.1007/978-94-015-9215-4.

35. Hilgenfeldt S, Grossman S and Lohse D, A simple explanation of light emission in sonoluminescence, *Nature* 398 (1999) pp. 402 – 405. https://doi.org/10.1038/18842.

36. Didenko YT, McNamara WB, Suslick KS, "Molecular emission from single bubble sonoluminescence", *Nature* 407 (2000) pp. 877 – 879. https://doi.org/10.1038/35038020.

37. Putterman SJ and Weninger KR, "Sonoluminescence: How Bubbles Turn Sound into Light", *Annual Review of Fluid Mechanics* 32 (2000) pp. 445 – 476. https://doi.org/10.1146/annurev.fluid.32.1.445.

38. Touchard G, "Streaming currents developed in laminar and turbulent flows through a pipe", *Journal of Electrostatics* 5 (1978) pp. 463 – 476. https://doi.org/10.1016/0304-3886(78)90038-4

39. Nelson JK, "Dielectric Fluids in Motion", *IEEE Electrical Insulation Magazine* 10:3 (1994) pp. 16 – 29. https://doi.org/10.1109/57.285419

40. Touchard G, "Flow electrification of liquids", *Journal of Electrostatics* 51-52 (2001) pp. 440 – 447. https://doi.org/10.1016/S0304-3886(01)00081-X

41. Leblanc P, Cabaleiro JM, Paillat T, Touchard G, "Impact of the laminar flow on the electrical double layer development", *Journal of Electrostatics* 88 (2017) pp. 76 – 80. https://doi.org/10.1016/j.elstat.2016.11.006

42. Mitroglou N, Gavaises E, Private Communication of Unpublished Data, City, University of London, 2018.

List of Figures

Figure 1: Layout of High-Pressure Recirculation Flow Rig.

Figure 2: Internal Design and Operation of a Generic Diesel Injector Pressure Control System.

Figure 3: Design Schematics of (a) Upstream, High-Pressure Fused Silica Element, and (b) Downstream, Low-Pressure Fused Silica Element.

Figure 4: Schematic of Fused Silica Model Diesel Injector Control System, Cage and Needle Screw Assembly.

Figure 5: Photograph of Recirculating Flow Rig, Model Injector Pressure Control Assembly, and Lens-Spectrometer Arrangement.

Figure 6: Photograph of Nikon D7000 DSLR camera and 50 mm f/1.2 lens reverse-coupled to lens extension tubes, and the Newport Oriel MS125 spectrometer and linear CCD array sensor.

Figure7: Colour Photograph of Hydrodynamic Luminescence occurring in the 2nd Nozzle of the Model Pressure Control Assembly.

Figure 8: False Colour Image of the Mean Luminescence obtained from 1,000 Image Frames captured sequentially at 2 kHz Frame Rate on the Photron FASTCAM SA1.1 Camera.

Figure 9: False Colour Image of the Standard Deviation obtained from 1,000 Luminescence Image Frames captured sequentially at 2 kHz on the Photron FASTCAM SA1.1 Camera.

Figure 10: Mean Spectral Signal Intensity (photo-electrons) as a Function of Wavelength (nm).

Figure 11: 2-Column Gas Chromatograph of the Diesel Sample Employed in this Test [19].

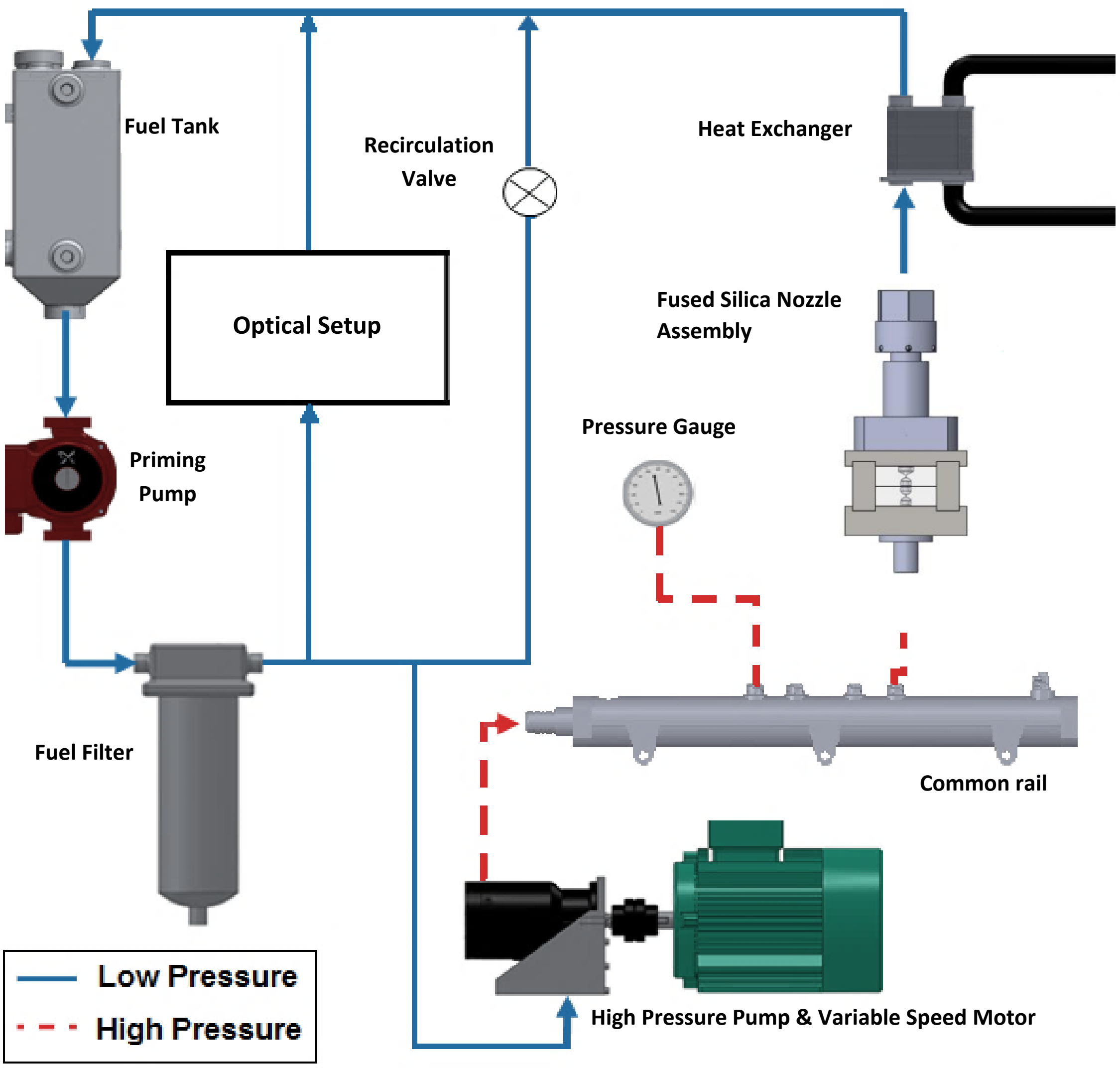

Figure 1: Layout of High-Pressure Recirculation Flow Rig with Fused Silica Nozzle Assembly

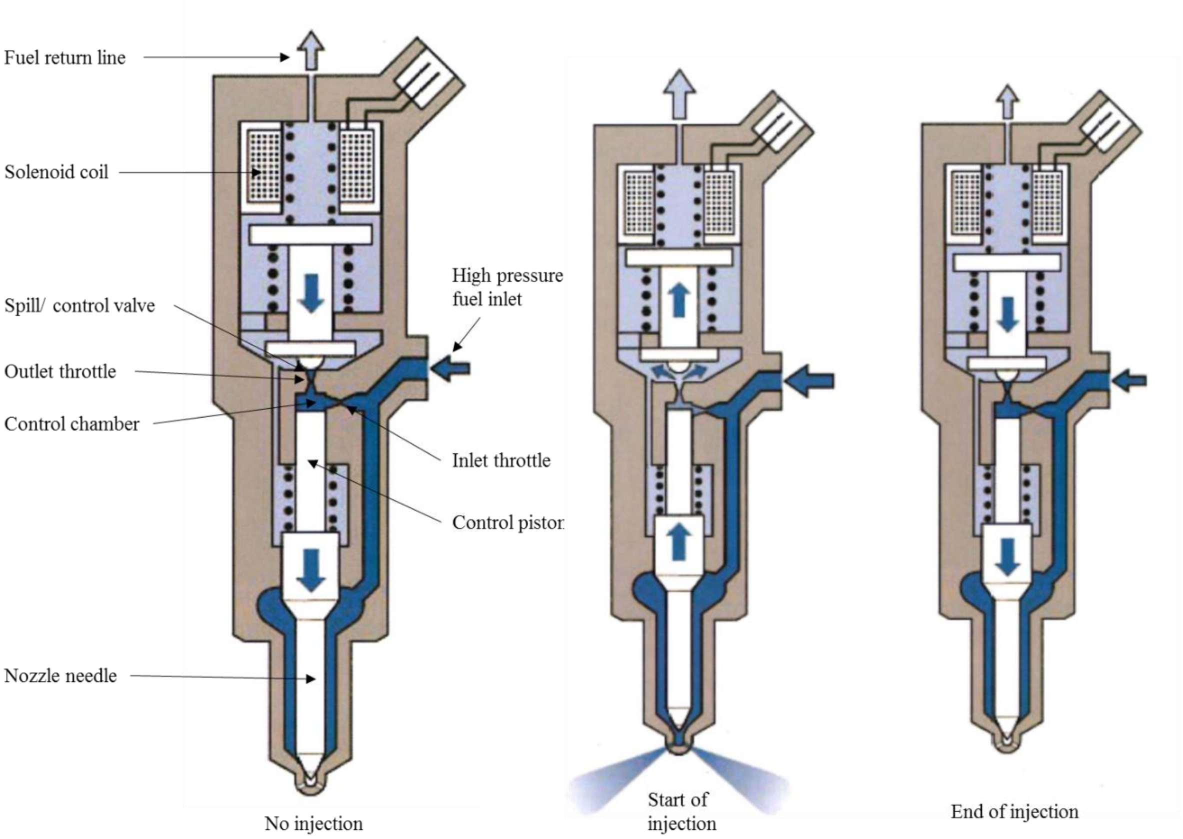

Figure 2: Internal Design and Operation of a Typical Diesel Injector Pressure Control System.

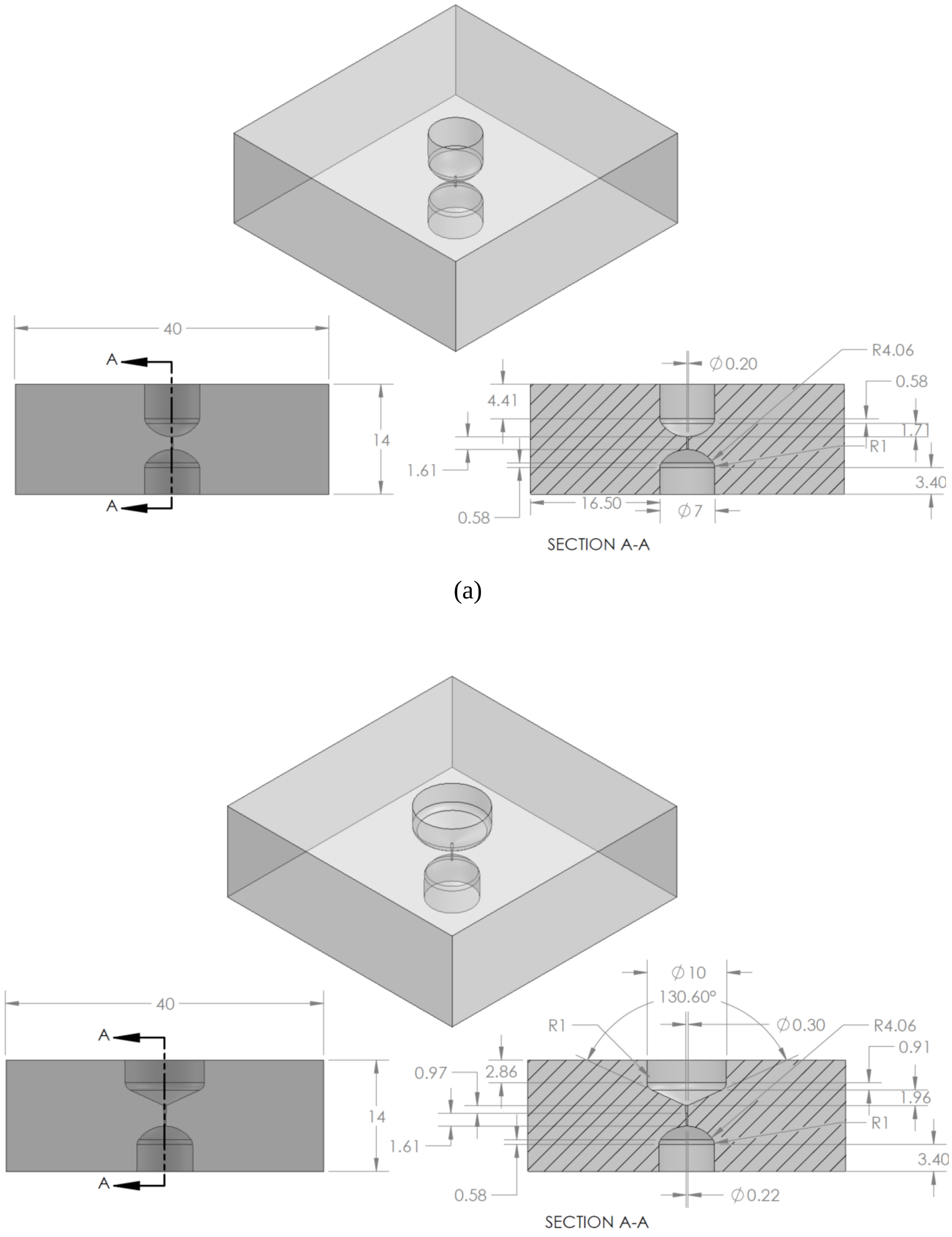

(a)

(b)

Figure 3: Design Schematics of (a) Upstream, High-Pressure Fused Silica Element, and (b) Downstream, Low-Pressure Fused Silica Element.

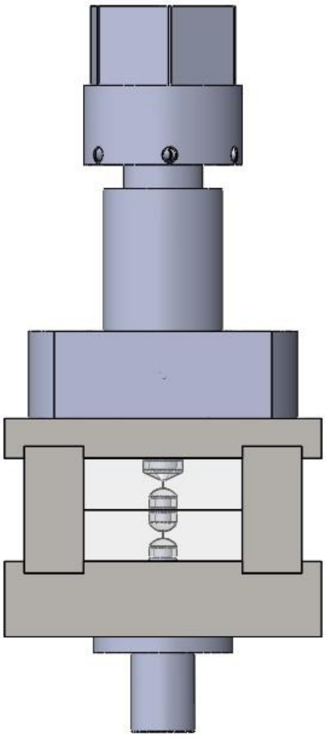

Figure 4: Schematic of Fused Silica Model Diesel Injector Control System, Cage and Needle Screw Assembly.

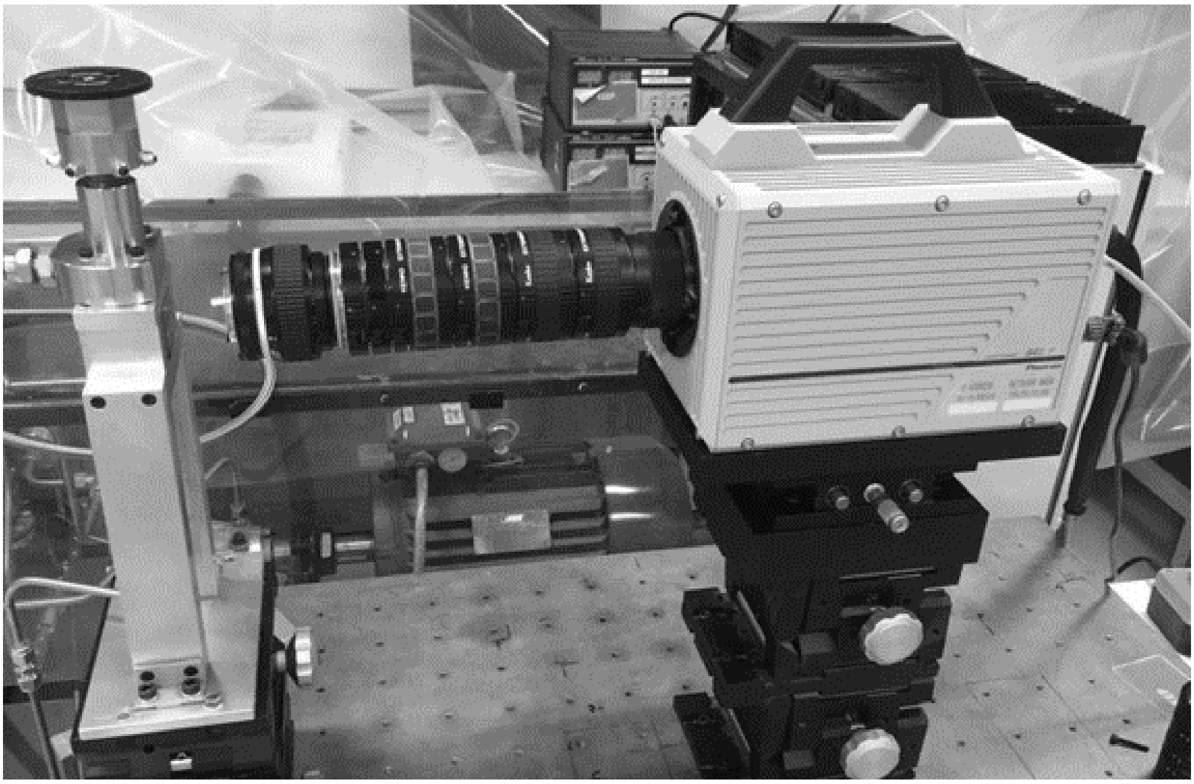

Figure 5: Photograph of Photron SA1.1 Video Camera, reverse-coupled to Nikon 50 mm f/1.2 Lens via 204 mm Lens Extension, focused on Hydrodynamic Luminescence originating from Fused Silica Model Diesel Injector Control System.

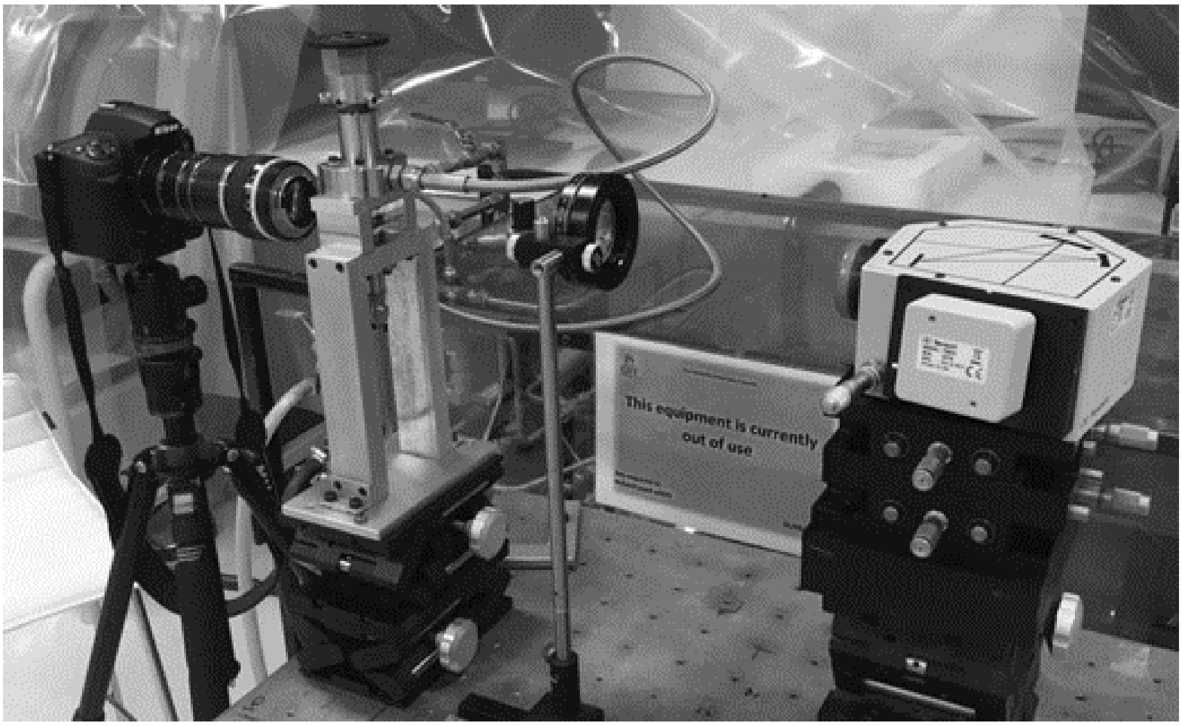

Figure 6: Photograph of Nikon D7000 DSLR camera and 50 mm f/1.2 lens reverse-coupled to lens extension tubes, and the Newport Oriel MS125 spectrometer and linear CCD array sensor.

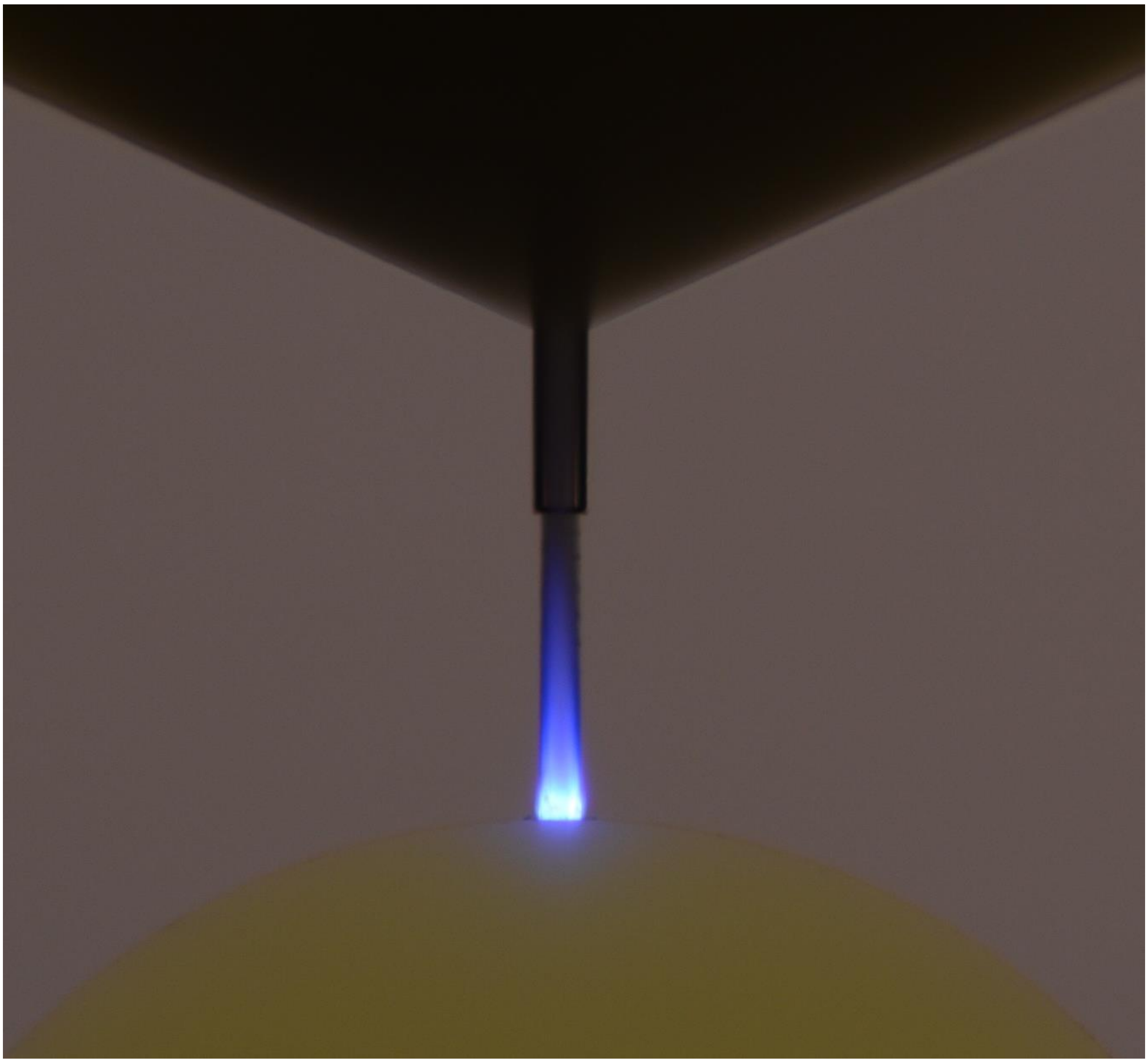

Figure 7: Colour Photograph of Hydrodynamic Luminescence occurring in the 2nd Nozzle of the Model Pressure Control Assembly.

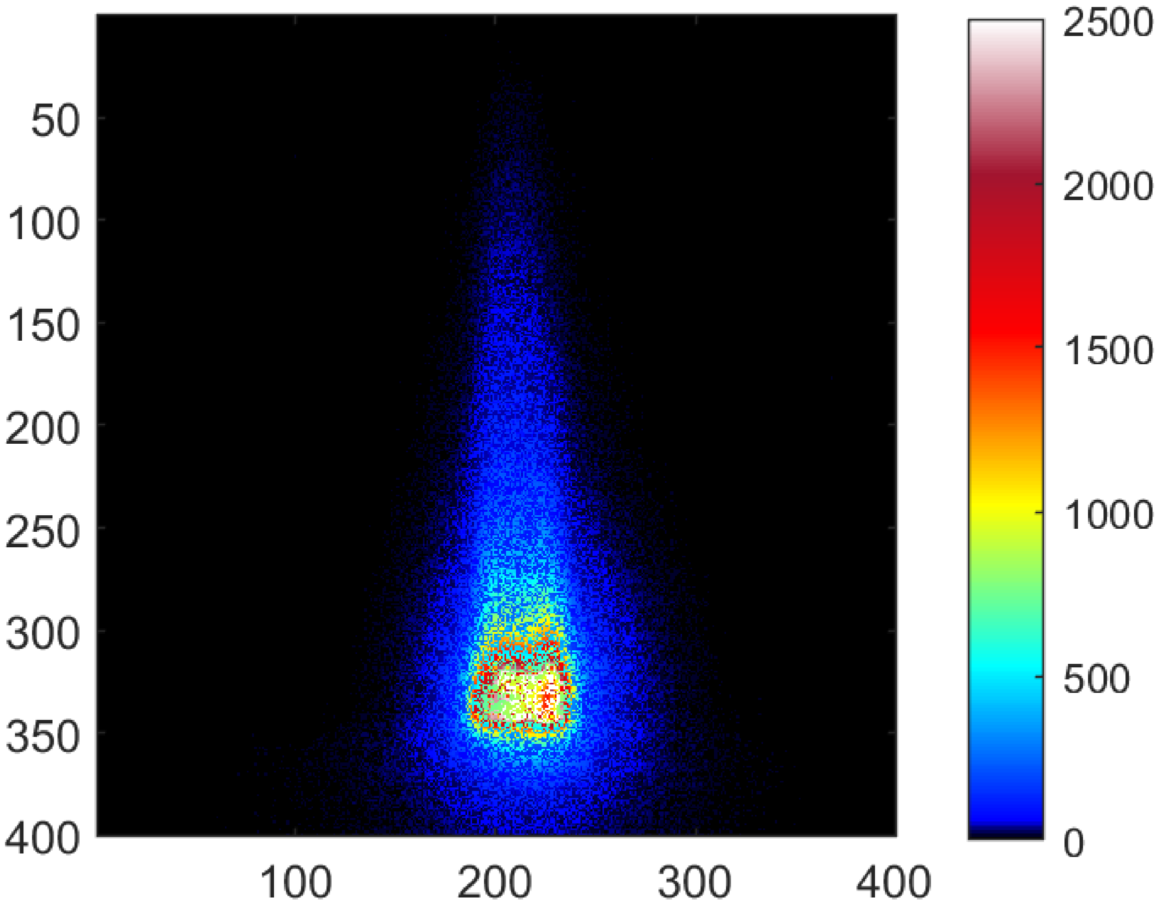

Figure 8: False Colour Image of the Mean Luminescence obtained from 1,000 Image Frames captured sequentially at 2 kHz Frame Rate on the Photron FASTCAM SA1.1 Camera.

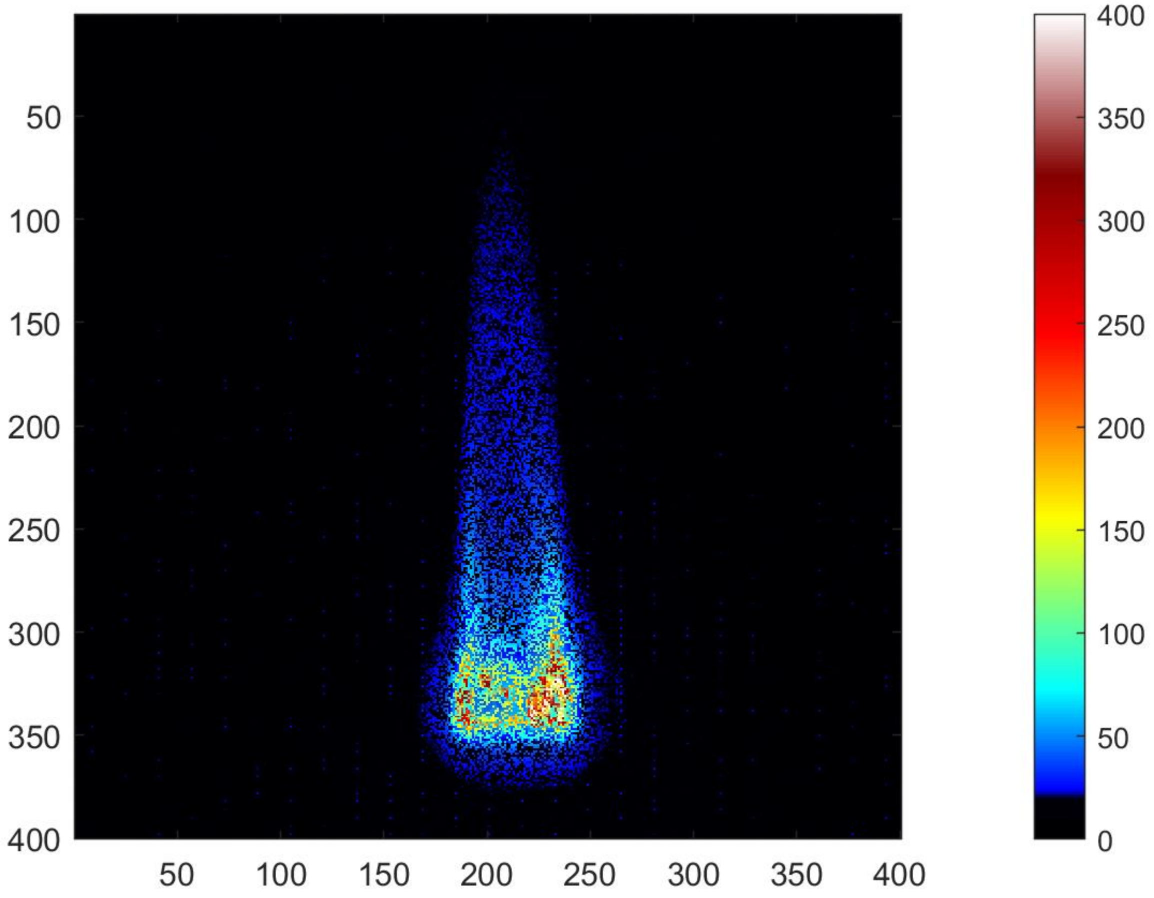

Figure 9: False Colour Image of the Standard Deviation obtained from 1,000 Luminescence Image Frames captured sequentially at 2 kHz on the Photron FASTCAM SA1.1 Camera.

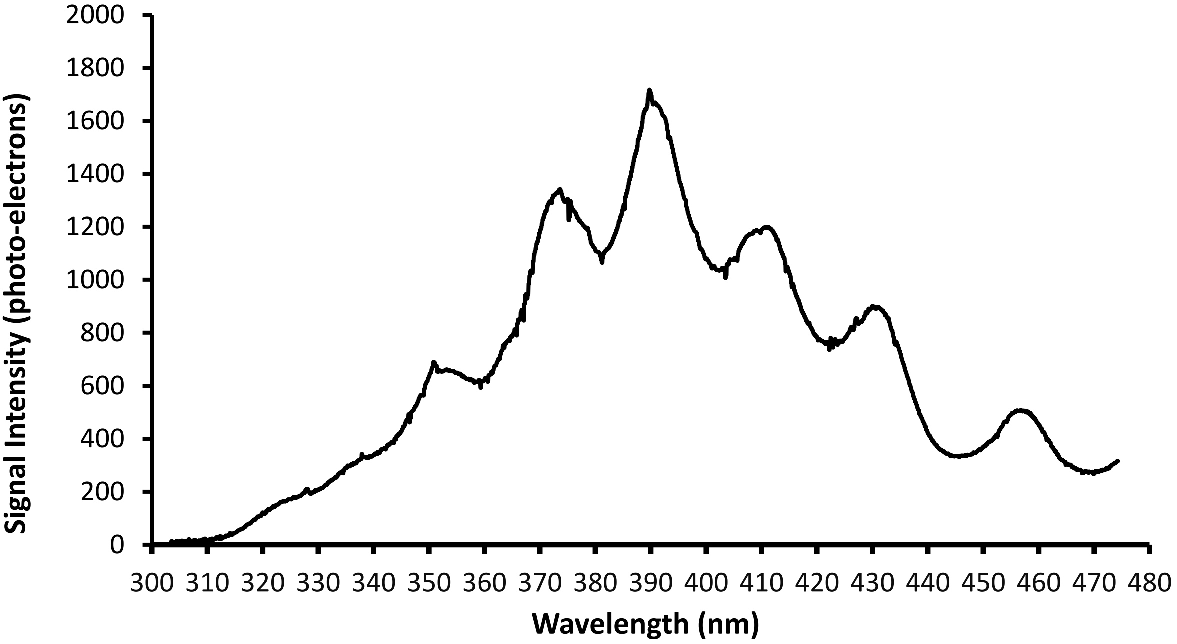

Figure 10: Mean Spectral Signal Intensity (photo-electrons) obtained from Diesel Luminescence Signal as a Function of Emission Wavelength (nm).

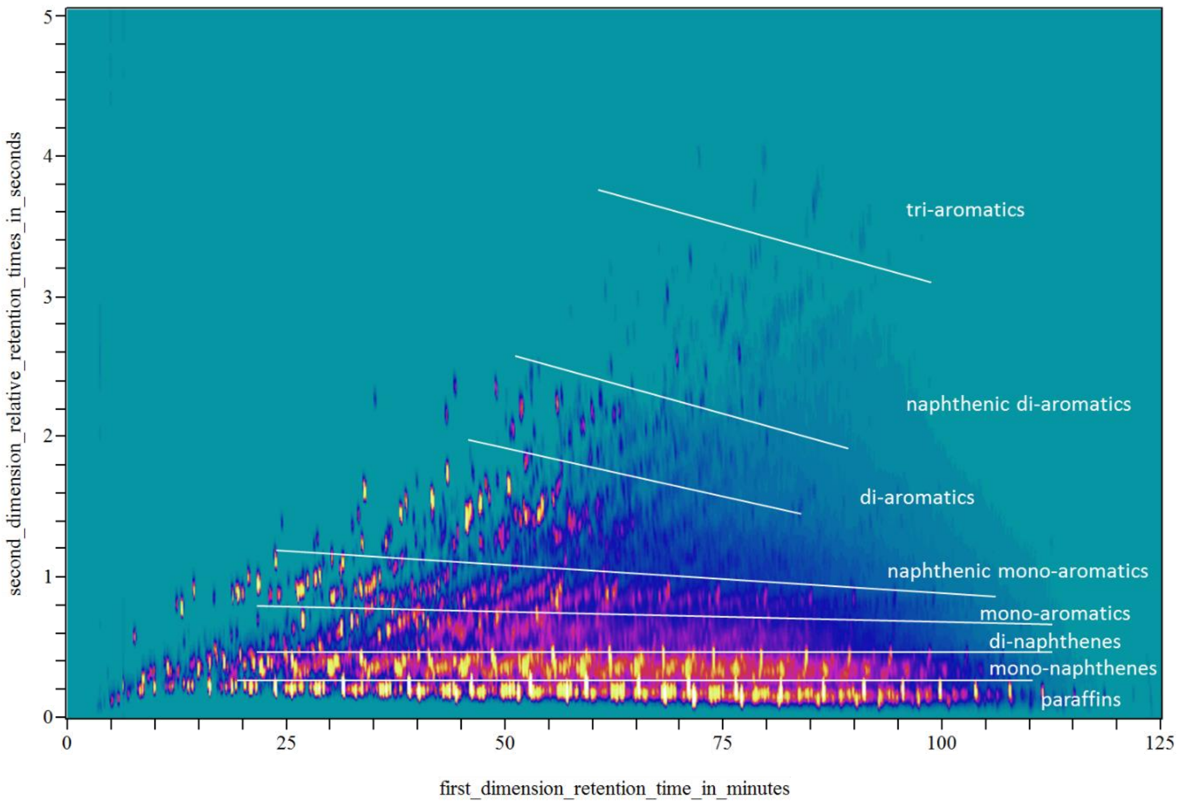

Figure 11: 2-Column Gas Chromatograph of the Diesel Sample Employed in this Test [19].